1 *Article*

2,3 Spatial Scales of Sea Surface Salinity Subfootprint Variability in the SPURS Regions

4 **Frederick M. Bingham[1]* and Zhijin Li[2]**

5 [1] University of North Carolina Wilmington, Department of Physics & Physical Oceanography;
6 binghamf@uncw.edu
7 ***** Correspondence: binghamf@uncw.edu
8 [2] Jet Propulsion Laboratory, California Institute of Technology; zhijin@jpl.nasa.gov
9

11 **Abstract:** Subfootprint variability (SFV), or representativeness error, is variability within the
12 footprint of a satellite that can impact validation done by comparison of in situ and remote sensing
13 data. This study seeks to determine the size of the SFV as a function of footprint size in two regions
14 that were heavily sampled with in situ data. The SPURS-1 (Salinity Processes in the Upper-ocean
15 Regional Studies) experiment was conducted in the subtropical North Atlantic in 2012-2013,
16 whereas the SPURS-2 study was in the tropical eastern North Pacific in 2016-2017. SFV was also
17 computed using a high-resolution regional model based on ROMS (Regional Ocean Modeling
18 System). We computed SFV at footprint sizes ranging from 20-100 km for both regions. SFV is
19 strongly seasonal, but for different reasons in the two regions. In the SPURS-1 region, the meso- and
20 submesoscale variability seemed to control the size of the SFV. In the SPURS-2 region, the SFV is
21 much larger than SPURS-1 and controlled by patchy rainfall.

25 1. Introduction

26   Sea surface salinity (SSS) has been measured by satellite for over 10 years from three different
27 platforms, ESA's SMOS (Soil Moisture and Ocean Salinity), NASA and CONAE's Aquarius and
28 NASA's SMAP (Soil Moisture Active Passive). The value of these measurements to the scientific
29 community and for practical applications has become clear over this time as has the need for
30 continuity. SMOS has been aloft since 2009 and, though still returning good data, is long past its
31 expected lifetime. Aquarius stopped transmitting in 2015. SMAP, also still returning good data, is
32 having to rely on ancillary measurements of sea surface roughness because its onboard scatterometer
33 stopped functioning soon after launch. Given all of this, there has been much interest in developing
34 new missions to measure SSS, and thus the need to understand the parameters of a such a mission.
35   Currently-used SSS sensors are passive microwave radiometers, and use a relatively long
36 wavelength of radiation to make their measurement. The measurements are thus averages over a
37 large footprint, 10s to 100s of kilometers depending on the frequency of radiation and configuration
38 of the satellite. Subfootprint variability (SFV) is the variance within the footprint of a satellite
39 measurement [1-3]. Because satellite SSS measurements are areal averages over a relatively large
40 footprint [4], and because existing validation is carried out by comparison to in situ point
41 measurements from floats, moorings and so on [5-9], there is a mismatch that can introduce error into
42 the validation process as explained in detail by [1]. The size of this error is beginning to be estimated
43 and understood [1-3, 10]. However, these important previous studies have been based on the
44 footprint the size of Aquarius, 100 km, whereas the SMAP and SMOS missions have smaller

45 footprints. The amount of SFV should depend on the size of the footprint, as well as many other
46 factors such as season, geographic location and the strength of mesoscale and submesoscale stirring
47 of the SSS field.
48   One of the most interesting results that has come out of the increased measurement of SSS over
49 the past decade is on the spatial scales of variability. While other surface variables measured by
50 satellite, namely sea surface temperature (SST) and sea surface height (SSH), have relatively large
51 scales [11-13], SSS variability occurs on a smaller scale [14]. Very high resolution numerical
52 modelling, with output focused on the western North Pacific and Arabian Sea [15], found that about
53 50% of open ocean SSS variance in these regions is on a scale of 50 km or less. That is, most ocean
54 variance occurs on a scale that is smaller than the footprint of Aquarius, and of similar size to that of
55 SMAP or SMOS.
56   This paper is an extension of [1], who assumed the footprint size to be a constant 100 km. In the
57 present work, we explore how SFV depends on footprint size, and begin to understand the dynamics
58 that cause SFV. The approach is to look at two heavily sampled regions, in which contrasting
59 dynamical processes are present, a couple of the small number places in the ocean where SFV can be
60 reliably determined using in situ data. We guess that SFV can be roughly related to 4 causes: (1)
61 rainfall-induced fresh patches (e.g. [16]); (2) internal ocean submesoscale and mesoscale variability
62 (e.g. [3, 17]); (3) large-scale fronts such as the North Equatorial Countercurrent (NECC) front that
63 moves between the equator and 10°N [17] and (4) mean gradients. These 4 causes are ordered roughly
64 in terms of scale from smallest to largest.
65   The two regions we are studying are SPURS-1 (Salinity Processes in the Upper Ocean Regional
66 Study – 1) and SPURS-2. SPURS-1 is a field campaign that took place in the subtropical North Atlantic
67 in 2012-2013 ([19] and references therein) centered on a mooring at (24.5°N,38°W). The SPURS-1 region
68 is evaporation-dominated with small gradients and weak currents. SPURS-2 took place in the tropical
69 eastern North Pacific in 2016-2017 ([20] and references therein) centered on a mooring at (10°N,125°W).
70 The SPURS-2 region is precipitation-dominated, with strong currents, and falls within the intertropical
71 convergence zone (ITCZ) for part of the year [21]. See [1] Figure 3 for the locations. We expect that SFV
72 will be induced mainly by cause (2) above in the SPURS-1 region and by causes (1)-(3) in the SPURS-2
73 region.

2. Data and Methods

75   This work uses the same dataset and methods as [1], and the reader is referred to section 2 of
76 that paper for a more detailed description than is given here.
77   For the SPURS-1 region we use a combination of drifter, waveglider and shipboard
78 thermosalinograph measurements [22] to compute estimates of SFV. In the SPURS-2 region [23], we
79 use waveglider measurements only – the region is too dynamic to make much use of drifter
80 measurements for this purpose, and the cruises were usually too distant from the location of the
81 central mooring to be useful. SFV is the square root of the weighted variance within a defined
82 footprint of size $2d_0$. In [1], the footprint size is fixed at 100 km, whereas here it is allowed to vary
83 from 20 to 100 km to determine the dependence of SFV on footprint size. Specifically, the SFV is
84 obtained from taking the square root of

$$\sigma^2 = \frac{\sum_C w_i (S_i - \bar{S})^2}{\sum_C w_i}$$

where the weight function w_i for each observation is

$$w_i = e^{-\ln(2)*(d_i/d_0)^2}$$

S_i is the observed SSS. The sum, C, is taken over all the observations being used to compute SFV
at a given point in time - SFV was computed over 7-day blocks of time. d_i is the distance of each

94 observation from the location of the central mooring, *i.e.* (24.6°N,38°W) for SPURS-1 and
95 (10°N,125°W) for SPURS-2. The weighted average SSS, $\bar{S}$, is
96

97
$$\bar{S} = \frac{\sum_C w_i S_i}{\sum_C w_i}$$

98
99 We display plots of median SFV, termed σ_{50}, as a function of footprint size over the approximately 1
100 year of available data at each site.
101   This paper uses the same ROMS (Regional Ocean Modeling System) [22, 24] output as was used
102 in [1], and the method of computing SFV is the same as for the in situ data.
103   Brief use is made of radar-derived rainfall collected during the SPURS-2 cruise in October-
104 November 2017. The data come from the Sea-viewing Polarimetric (SEA-POL) radar described by
105 [25, 26]. Brief use is also made of rainfall data collected at the SPURS-1 and SPURS-2 central moorings
106 [27, 28]
107   A list of digital object identifier (DOI) references to the datasets used in this paper is included in
108 the Acknowledgements section.
109

110 **3. Results**

111 *3.1. In situ results*

112   Time series of SFV (Figure 1) in the SPURS regions indicate that it is a seasonal quantity, tending
113 to be largest in summer and fall (June-December) and smallest in winter and spring (January-May).
114 SFV in the SPURS-2 region is larger than SPURS-1, though the difference is least in the low variance
115 season. In most instances, SFV is larger at the 100 km footprint size for both regions. There are isolated
116 time periods when this is reversed, especially in the SPURS-1 region. There tends to be a larger
117 distinction as a function of scale for the SPURS-1 region. That is, for SPURS-1, the ratio of 100 km SFV
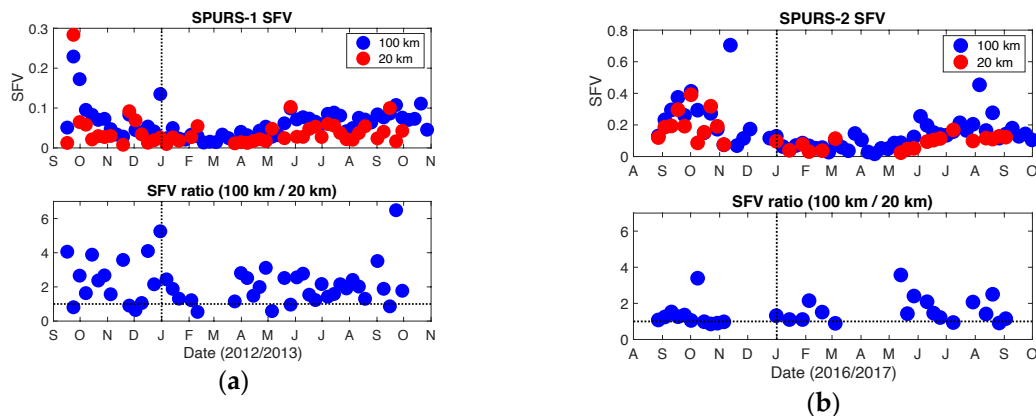118 to 20 km SFV is generally larger than for SPURS-2.

119 **Figure 1.** Time series of SFV in the SPURS regions. Top panels: Blue markers are SFV using a 100 km
120 footprint size. Red markers use a 20 km footprint. Bottom panels: Ratio of 100 km to 20 km SFV. That
121 is, the ratio of the blue markers in the top panels to the red markers. The horizontal dashed line
122 indicates where this ratio is 1. (**a**) SPURS-1; (**b**) SPURS-2. Note vertical axes are not consistent between
123 the top panels.

124   The findings from the time series are presented in simpler form using σ_{50} (Figure 2). As also seen
125 in Figure 1, SFV is as much as 4X larger at SPURS-2 than SPURS-1. At SPURS-1, SFV increases with
126 footprint size from 20 to 60 km, and then levels off at around 0.05. At the SPURS-2 site, SFV does not
127 increase at all from 20 to 60 km, and then increases a little bit. There is proportionally much less
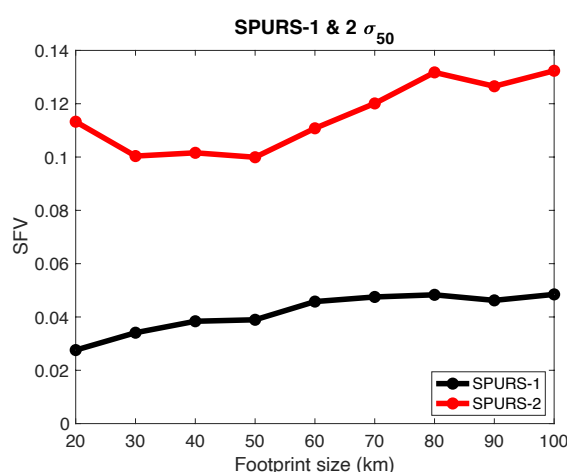128 dependence on footprint size at SPURS-2 than SPURS-1, in agreement with Figure 1.

Figure 2. σ_{50} as a function of footprint size for SPURS-1 (black) and SPURS-2 (red) in situ data.

In the SPURS-1 region there is little rainfall between March 1 and August 31 [27], and in the SPURS-2 region between February 1 and May 31 [28]. (Henceforth we use months in an inclusive sense. That is, "March-August" means March 1 – August 31.) Additionally, at the SPURS-2 site, the NECC front is well south of the mooring during those "dry" months [21]. So, for both sites, one can assume that any SFV there during these periods is due to internal variance within the ocean and not imprinted directly by the atmosphere through precipitation. Evaporation may imprint some SFV, but not likely much as SSS anomalies imposed by evaporation tend to dissipate quickly [29].

Separating the SFV out during the wet and dry periods (Figure 3), one can see a sharp contrast between the regions. In the SPURS-1 region, SFV increases strongly with footprint size from 20 to 70 km during the dry season, but only out to 40 km in the wet season. SFV is about the same between wet and dry seasons to 40 km. At larger footprint sizes, it is counterintuitively much larger during the dry season. The dry season corresponds to spring and summer, so one has to assume that internal variability is larger during these months than during fall and winter at 50+ km length scales. This seems consistent with [30] who found elevated eddy kinetic energy (EKE) in the SPURS-1 region during the months of April-September. Larger EKE presumably means stronger eddy activity at the mesoscale, and thus larger variability of SSS at that scale as well.

At the SPURS-2 site, the situation is very different. Wet season SFV is much larger than dry season. Dry season median SFV is comparable between the two regions at the largest (70-100 km) scales, but smaller in the SPURS-1 region at smaller scales.

It should be noted that the dry season and the low SFV season are not the same for the SPURS-1 region. The dry season is March – August, whereas the low SFV season is approximately January – April (Figure 1a). On the other hand, the dry season and low SFV season do mostly overlap for the SPURS-2 region. This suggests that there is seasonal variability inherent to the ocean at the SPURS-1 site that may be more important than rainfall in determining the size of SFV. A similar plot separating high SFV and low SFV seasons at the SPURS-1 site is presented in Figure 4. This may be a more logical way of separating parts of the year for SPURS-1, and shows the variation of SFV with scale, which is consistent between low SFV and high SFV seasons. Both curves level off at around 70 km footprint size.
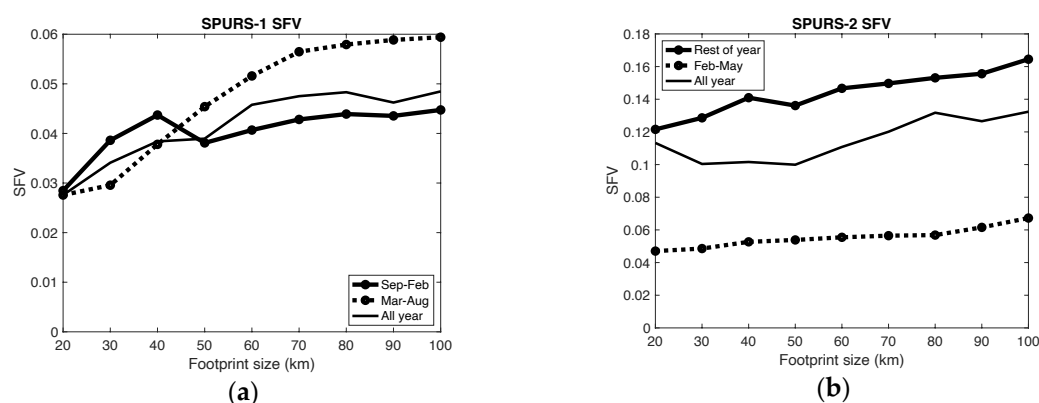
(**a**) (**b**)

Figure 3. Median SFV vs. footprint size in the SPURS regions. Solid lines with markers: wet season. Thinner solid lines with no markers: all year, same as curves shown in Figure 2. Dashed lines with markers: dry season. (**a**) SPURS-1. Dry season is March – August. (**b**) SPURS-2. Dry season is February – May. Note vertical axes are not consistent between the panels.
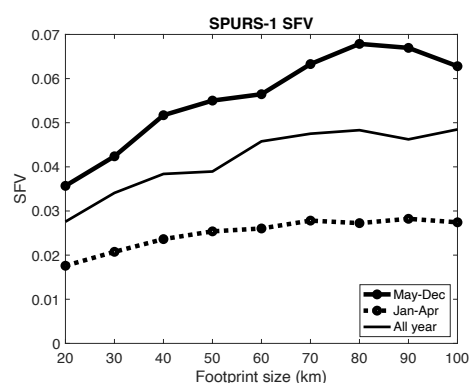

Figure 4. As in Figure 3a. However, the dashed line is for January – April, and the solid line with symbols is for the rest of the year, May - December.

In the SPURS-2 region, the fact that the wet season SFV is so much larger than the dry season may be related to either (1) increased precipitation, and thus imprinted small scale variability, (2) the migratory presence of the NECC front during the summer and fall [18], (3) seasonally increased mesoscale variability – or (4) some combination of these. Distinguishing these factors is not easy. One clue is the fact that there is not much dependence of SFV on scale. If rainfall is ubiquitous during these months, and it produces small fresh patches throughout the region (a typical example is shown in Figure 5), and if SFV can be enhanced by even one fresh patch in a given snapshot, then that argues for the importance of rainfall in determining SFV. In other words, if the scale of rain-induced fresh patches is smaller than the 20 km we have been studying here and most SSS variance is due to these patches, then we would see less scale dependence of SFV as is the case at the SPURS-2 site. It is harder to make such an argument for the NECC front. As footprint size increases it has an increased probability of encompassing the front, and thus should have a strong dependence on scale.
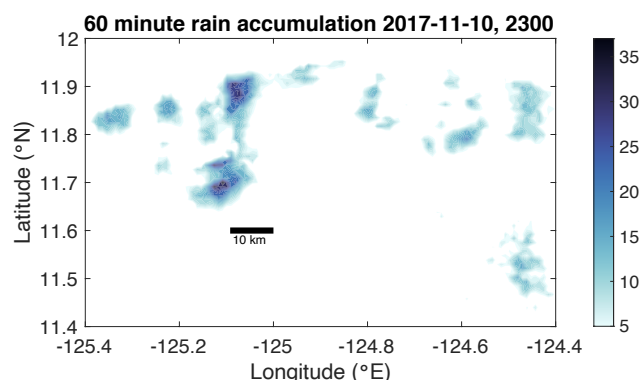
Figure 5. 60-minute rain accumulation (mm) from the SPURS-2 cruise on 11-November-2017 at 2300Z. No color means less than 5 mm. The data are from the SEA-POL radar used during the cruise [25, 26]. This is a typical configuration of rainfall in the region at this time of year. A bar showing 10 km distance is also included. The location of this area is shown in [1], Figure 3b.

We can test whether SFV depends on precipitation by plotting SFV against 7-day maximum rain rate (Figure 6). The scatter plots show a clear relationship between rain rate and SFV even though the precipitation data used to make these plots are from the SPURS central moorings, and thus may not be representative of the entire footprint. So, in both regions there is evidence that rainfall plays at least some role in generating SFV at a range of spatial scales. The larger the scale, the greater the correlation between SFV and rainfall. Interestingly, the correlations are higher for the SPURS-1 region, where rainfall is much smaller, than for the SPURS-2 region. The results of Figure 3a and Figure 6a seem contradictory at first glance, but one must remember that the points in Figure 6a only represent the wet season.
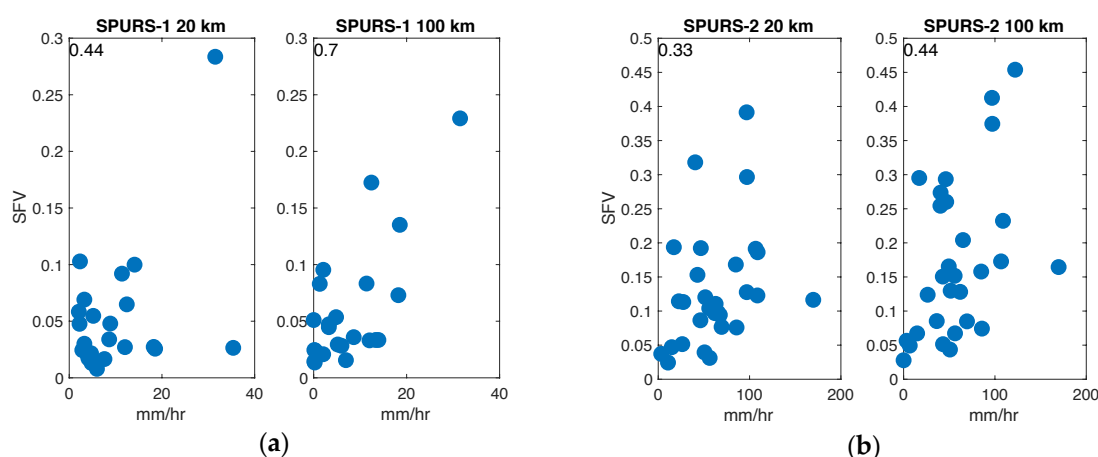

Figure 6. SPURS SFV vs. maximum rain rate measured at the central mooring when this value exceeds 2 mm/hr. Maximum rain rate was determined over the same weekly time intervals as the SFV. Correlation values are shown at the top left of each panel. All are significant at the 95% level, except for SPURS-1 at 20 km which is significant at the 90% level. Left panels: 20 km footprint size. Right panels: 100 km footprint size. (a) SPURS-1. (b) SPURS-2. Note vertical axes are not consistent between the panels.

To understand the spatial variability better, semivariograms were plotted (Figure 7) using the in situ data from each site from the simple estimator [31]

$$\hat{\gamma}(v) = \frac{1}{2N(v)} \sum_{N(v)} \left(S(x_i) - S(x_J) \right)^2$$

Where $S(x_i)$ is the salinity at point x_i and $N(v)$ is the number of pairs of salinity values where the distance between them is v.
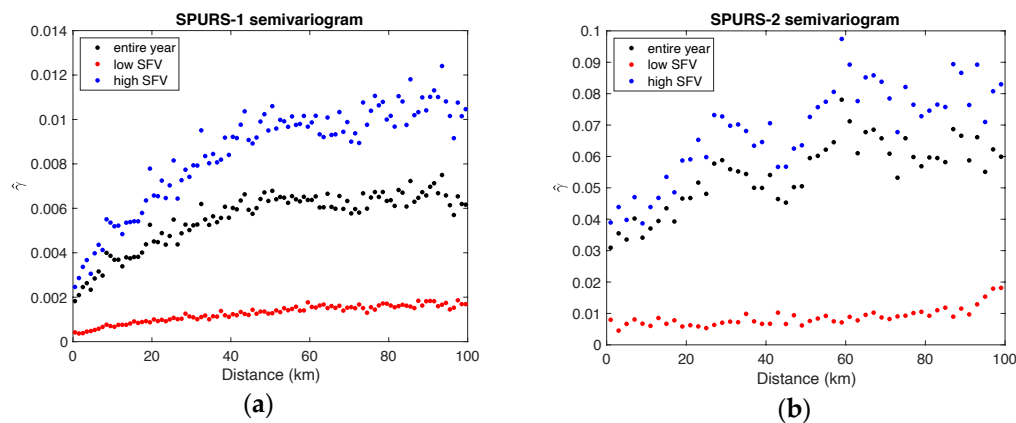

(**a**)   (**b**)

Figure 7. Semivariograms as a function of distance computed from in situ data. (**a**) SPURS-1. Red symbols, January – April. Black symbols: Entire year. Blue symbols: May - December. (**b**) SPURS-2. Red symbols, February – May. Black symbols: Entire year. Blue symbols: June - January. Note vertical axes are not consistent between the panels.

The semivariogram shows the scales of variability. This function is closely related to the spatial covariance as explained by [31]. It is the mean squared difference between values as a function of spatial separation. The semivariogram value at zero separation, the "nugget" in the parlance of [31], normally describes a kind of instrumental error. In this case, as these values were computed using 7-day snapshots, the nugget is the variance over a 7-day period.

The semivariograms for SPURS-1 are much as one would expect, with small values at small separation, increasing to a plateau (the "sill") at 50 km or so (the "range"). The semivariogram during the low SFV period is much smaller, but it contains the same dependence on separation distance.

The semivariogram at SPURS-2 is very different. It appears to increase from 0 to 20 km during the wet season, reaches a plateau, and then becomes very noisy at a distance beyond that. Thus, a rough estimate of the decorrelation scale is that 20 km. During the dry season (red symbols), though, it appears that there is almost no dependence of the semivariogram on scale, because of the way the axes are presented in Figure 7, it does actually increase. Despite this, there is no obvious sill or range during the dry season.

3.2. ROMS Results

Time series of SFV computed from the ROMS (Figure 8) contrast the two regions, and show the difference between model and the in situ results presented in the previous section. It should be noted here that the model encompasses a somewhat different time period than the in situ data collection. For SPURS-1, the model covers January 1, 2012 – December 31, 2012, whereas the field campaign lasted from September 2012 to September 2013, thus overlapping by 4 months. For SPURS-2, the model covers February 1, 2017 – January 31, 2018, whereas the field campaign went from August 2016 to November 2017, giving ~9 months of overlap.

236   The SPURS-1 model output has similar seasonality as the in situ results (Figures 1 and 4).
237 Minimum values of SFV are in February-June. The sizes match more or less the ones presented in
238 Figure 2 for 20 km footprint size, but ROMS shows a larger value of SFV for 100 km footprint size
239 than in situ, ~0.08 vs. 0.05. At almost no time does the 20 km SFV exceed the 100 km as shown in
240 Figure 1a. The 100 km time series is smoother than the 20 km one. Thus, the separation of SFV by
241 scale seen in the in situ data (Figure 4) is also evident in the ROMS results, but to a greater degree.
242

244   **Figure 8.** ROMS-evaluated SFV for SPURS-1 (upper) and SPURS-2 (lower). Red (blue) curves are for
245   100 km (20 km) footprint size.

246
247   For SPURS-2, the results are different. Values of SFV at 20 km fluctuate, but on short time scales
248 and little seasonality is evident. The 20 km SFV is much smaller (~0.03) than the median in situ value
249 of Figure 2 (~0.12). At 100 km, the SFV from ROMS (~0.1) is still smaller than the in situ value (~0.13),
250 but not by as much. Not much seasonality is evident at 100 km either, though SFV is slightly elevated
251 in July-September. There is some change in the time scales of variability of SFV. The time series of
252 100 km SFV fluctuates much more rapidly after the beginning of July than before. There is a clear
253 separation of scale for the SPURS-2 region as there was for SPURS-1.
254   These results are summarized in Figure 9. Strikingly, the two curves of Figure 9 from the
255 different SPURS regions are very similar in contrast to Figure 2. Both show a stronger increase of SFV
256 as a function of spatial scale than is seen in Figure 2. SFV at 100 km is somewhat less for SPURS-1
257 than SPURS-2, but they are nearly the same at smaller scales. The SPURS-2 region has a smaller
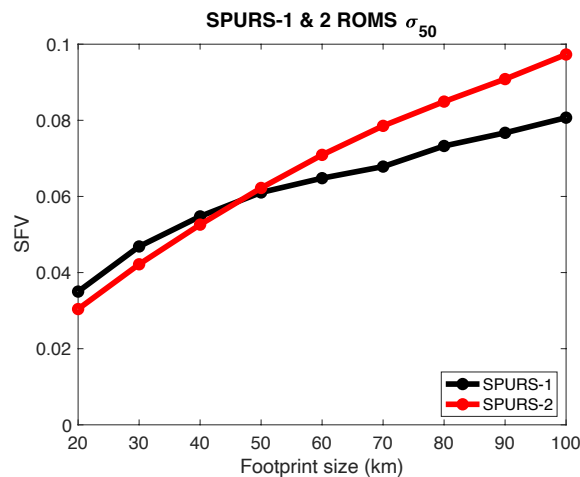258 separation as a function of season than SPURS-1 (Figure 9).
259

Figure 9. As in Figure 2, but for ROMS output.

One of the main differences between the model and the real ocean is the forcing. The ocean is forced with rainfall that occurs in small, patchy bursts, especially in the SPURS-2 region (Figure 5; [25, 26, 32, 33]). These bursts create rain puddles on kilometer scales [16]. ROMS is forced with 18 km NCEP (National Centers for Environmental Prediction) GFS (Global Forecast System) winds and precipitation [24], and thus lacks the small-scale variability in freshwater forcing which could lead to large values of SFV. Perhaps this is what causes the relatively small SFV and lack of seasonality in the SPURS-2 results especially at short spatial scales. SFV in ROMS may be mainly a measure of ocean variability, not variability imposed externally by patchy rainfall. Thus, the black curve in Figure 8 for SPURS-1 is similar to the (dashed) one for the dry season in Figure 3a. There is no such similarity for SPURS-2. The relatively smaller amount of seasonality in ROMS than in the in situ data supports the role of small rain patches in generating SFV.
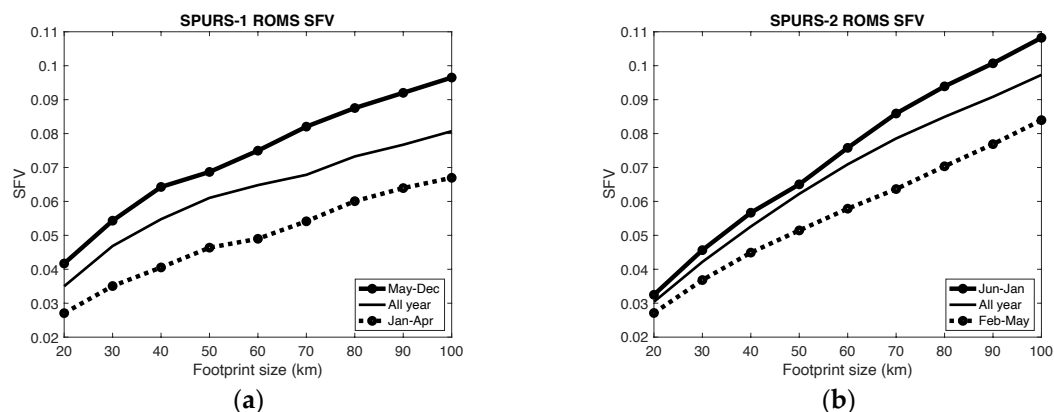

Figure 10. a) As in Figure 4, but with SFV computed from the ROMS simulation. b) As in Figure 3b, but with SFV computed from the ROMS simulation. Light black curves are the same as those displayed in Figure 8.

4. Discussion

We have explored SFV in two different regions and found that it varies by scale differently in each place. We have used two tools to make these conclusions. The first is an in situ dataset of drifters, shipboard measurements and wavegliders for SPURS-1 and wavegliders only for SPURS-2 [1]. The second is high-resolution regional simulations. Neither of these tools is perfect. The in situ data are not comprehensive in areal and temporal coverage and contain a mixture of skin surface and bulk

285 mixed layer observations. This may be a bigger issue in the SPURS-2 region because rain events
286 produce thin low salinity layers there [16, 34, 35]. The model lacks completely realistic forcing. It may
287 be missing mixed-layer dynamics that are important in determining or hindering the ability of fresh
288 patches to be incorporated into the bulk mixed layer and in turn affect the statistics of horizontal
289 variability, again especially in the SPURS-2 region [36].
290   Comparison of the two regions is illuminating though. In general, the SPURS-2 region has much
291 higher SFV than SPURS-1 (Figure 2), as determined from in situ data. (Model results are different –
292 Figures 9 and 10.) Another result is that SFV in the SPURS-1 region has a stronger scale dependence
293 than that of SPURS-2, especially in the high SFV season (compare top curves in Figures 3b and 4).
294 The SPURS-1 SFV has clear plateaus at 60+ km in all seasons (Figures 4 and 7), whereas the scale
295 dependence in SPURS-2 increases continuously as a function of footprint size (Figures 3b and 7).
296   The scales of variability are straightforward to compute and interpret for SPURS-1. For SPURS-
297 2, doing this requires a more detailed analysis than has been attempted here. Possibly, SSS variability
298 is not isotropic in low latitudes and has different scales in the zonal and meridional directions, though
299 this is not the conclusion of [37]. Research is ongoing into this.
300   In terms of design of future satellite missions, one can use Figures 2, 3b and 4 to get an idea of
301 how much SFV to expect for a given footprint. The size of a footprint is determined by the frequency
302 of radiation being measured, the diameter of the antenna, the height of the satellite above the Earth,
303 etc., parameters which can be determined in the design phase of a satellite. The numbers displayed
304 in Figures 2, 3b and 4 can be factored into error budgets for future missions, remembering that error
305 associated with SFV is just a mismatch of scales between in situ validation measurements and
306 footprint average values [1]. More importantly, the results presented here give a sense of how much
307 variability is being captured by a given footprint. If one wanted to capture scales of variability smaller
308 than the mesoscale, that would mean a smaller than ~50-100 km footprint in mid-latitude and larger
309 in the tropics [38]. Microwave SSS sensors are more sensitive in the tropics because of the warmer
310 temperatures [4]. If the large SFV of 0.12-0.16 in the wet season is factored in, the accuracy of the
311 retrievals may be better than previously thought there.
312   This study highlights the complexity of SFV, with its spatial and temporal dependence. No area
313 of the ocean is the same. The two regions we have studied may be thought of as open ocean extremes.
314 The SPURS-1 region is extreme for high evaporation, high SSS and low precipitation. The SPURS-2
315 region has heavy and patchy rainfall (Figure 5), strong and seasonally-varying currents and
316 associated frontal features [21]. Ideally, one would wish to quantify SFV over the entire and less
317 extreme open ocean in order to better characterize the error structure of satellite-derived SSS. This
318 would involve many more SPURS-like experiments. Unfortunately, this is not practically possible
319 and so we are left with guessing at its magnitude. Another possibility would be to use high-resolution
320 models to make estimates of SFV over the ocean. One of the main purposes of the present work is to
321 examine the potential for this. Research is ongoing [15], but the results of this present study suggest
322 caution. The model used here, though it is state-of-the-art, does not appear to get the distinction
323 between the regions correct – compare Figures 2 and 9. It also does not present the same level of
324 seasonality in SFV as we see in the in situ data – compare Figures 3b, 4 and 10.

5. Conclusions

326   From in situ data, it appears that at the SPURS-1 site, SFV is mainly generated by internal ocean
327 variability since its seasonality is unrelated to that of precipitation in the region. SFV at SPURS-1 is
328 highly seasonal, being largest in May-December and may be related to seasonality of the energy of
329 the mesoscale eddy field. Assuming SFV is produced by the eddy field, it is scaled to the typical size
330 of mesoscale variations, about 50-70 km.
331   At the SPURS-2 site, SFV is likely mostly produced by rainfall, whose scales are less than 20 km
332 (Figure 5). It is also highly seasonal, with maximum values during the rainy (wet) season, June-
333 January. At the scales examined, SFV showed little dependence on scale. The semivariograms
334 examined in Figure 6 suggest that much of that dependence is contained within the shortest (<20 km)
335 scales.

336   SFV is many times larger at the SPURS-2 site than at SPURS-1 (Figures 2, 3b and 4) at all footprint
337 sizes. This highlights the fact that SFV is highly spatially dependent, and any study of the error
338 associated with SFV needs to take that into account. There are very few areas in the open ocean that
339 have been sampled as intensively for SSS as the SPURS regions. In order to get a full understanding
340 of SFV error we must develop proxies which can stand in for the heavy sampling of the SPURS
341 regions. We have attempted to do that here by examining two ROMS simulations. The one in the
342 SPURS-1 region does a reasonable job of depicting the size and spatial dependence of SFV. In the
343 SPURS-2 region, the simulation is less realistic, likely due to the lack of small-scale rainfall.
344

References

1.   Bingham, F.M. Subfootprint Variability of Sea Surface Salinity Observed during the SPURS-1 and SPURS-2 Field Campaigns. *Remote Sensing* **2019**, *11*, 2689, doi:10.3390/rs11222689.
2.   Boutin, J.; Chao, Y.; Asher, W.E.; Delcroix, T.; Drucker, R.; Drushka, K.; Kolodziejczyk, N.; Lee, T.; Reul, N.; Reverdin, G. Satellite and in situ salinity: understanding near-surface stratification and subfootprint variability. *Bulletin of the American Meteorological Society* **2016**, *97*, 1391-1407, doi:10.1175/BAMS-D-15-00032.1.
3.   Drushka, K.; Asher, W.E.; Sprintall, J.; Gille, S.T.; Hoang, C. Global patterns of submesoscale surface salinity variability. *Journal of Physical Oceanography* **2019**, *49*, 1669-1685, doi:10.1175/JPO-D-19-0018.1.
4.   Lagerloef, G.S.; Colomb, F.R.; Le Vine, D.M.; Wentz, F.; Yueh, S.; Ruf, C.; Lilly, J.; Gunn, J.; Chao, Y.; deCharon, A., et al. The Aquarius/SAC-D Mission: Designed to Meet the Salinity Remote-sensing Challenge. *Oceanography* **2008**, *20*, 68-81.
5.   Abe, H.; Ebuchi, N. Evaluation of sea-surface salinity observed by Aquarius. *Journal of Geophysical Research Oceans* **2014**, *119*, 8109-8121, doi:10.1002/2014JC010094.

6.   Kao, H.-Y.; Lagerloef, G.S.; Lee, T.; Melnichenko, O.; Meissner, T.; Hacker, P. Assessment of Aquarius Sea Surface Salinity. *Remote Sensing* **2018**, *10*, 1341, doi:10.3390/rs10091341.

7.   Bao, S.; Wang, H.; Zhang, R.; Yan, H.; Chen, J. Comparison of Satellite-Derived Sea Surface Salinity Products from SMOS, Aquarius, and SMAP. *Journal of Geophysical Research: Oceans* **2019**, *124*, 1932-1944, doi:10.1029/2019jc014937.

8.   Fore, A.; Yueh, S.; Tang, W.; Hayashi, A. *SMAP Salinity and Wind Speed Users Guide, Version 4.3*; California Institute of Technology: Pasadena, CA, 2020; p 259.

9.   Qin, S.; Wang, H.; Zhu, J.; Wan, L.; Zhang Y.; Wang H. Validation and correction of sea surface salinity retrieval from SMAP. Acta Oceanologica Sinica, 2020, 39(3): 148–158, doi: 10.1007/s13131-020-1533-0.

10.   Vinogradova, N.T.; Ponte, R.M. Small-scale variability in sea surface salinity and implications for satellite-derived measurements. *Journal of Atmospheric and Oceanic Technology* **2013**, *30*, 2689-2694, doi:10.1175/JTECH-D-13-00110.1.

11.   Jacobs, G.A.; Barron, C.N.; Rhodes, R.C. Mesoscale characteristics. *Journal of Geophysical Research* **2001**, *106*, 19581-19595, doi:10.1029/2000JC000669.

12.   Kuragano, T.; Kamachi, M. Global statistical space-time scales of oceanic variability estimated from the TOPEX/POSEIDON altimeter data. *Journal of Geophysical Research* **2000**, *105*, 955-974, doi:10.1029/1999JC900247.

13.   Meyers, G.; Phillips, H.; Smith, N.; Sprintall, J. Space and time scales for optimal interpolation of temperature — Tropical Pacific Ocean. *Progress in Oceanography* **1991**, *28*, 189-218, doi:10.1016/0079-6611(91)90008-A.

14.   Bingham, F.M.; Lee, T. Space and time scales of sea surface salinity and freshwater forcing variability in the global ocean (60° S–60° N). *Journal of Geophysical Research: Oceans* **2017**, *122*, 2909-2922, doi:10.1002/2016JC012216.

15.   D'Addezio, J.M.; Bingham, F.M.; Jacobs, G.A. Sea surface salinity subfootprint variability estimates from regional high-resolution model simulations. *Remote Sensing of Environment* **2019**, *233*, 111365, doi:10.1016/j.rse.2019.111365.

16.   Drushka, K.; Asher, W.E.; Jessup, A.T.; Thompson, E.J.; Iyer, S.; Clark, D. Capturing Fresh Layers with the Surface Salinity Profiler. *Oceanography* **2019**, *32*, doi:10.5670/oceanog.2019.215.

17.   Hasson, A.; Farrar, J. T.; Boutin, J.; Bingham, F.; Lee, T. Intraseasonal variability of surface salinity in the eastern tropical Pacific associated with mesoscale eddies. *Journal of Geophysical Research: Oceans* **2019**, 124, 2861– 2875. doi:10.1029/2018JC014175.

18.   Yu, L. Sea-surface salinity fronts and associated salinity-minimum zones in the tropical ocean, *Journal of Geophysical Research: Oceans* **2015**, 120, 4205–4225, doi:10.1002/2015JC010790.

19.   Lindstrom, E.; Bryan, F.; Schmitt, R. SPURS: Salinity Processes in the Upper-ocean Regional Study. *Oceanography* **2015**, *28*, 14, doi:10.5670/oceanog.2015.01.

20.   Lindstrom, E., J.; Edson, J.B.; Schanze, J.J.; Shcherbina, A.Y. SPURS-2: Salinity Processes in the Upper-Ocean Regional Study 2 – The Eastern Equatorial Pacific Experiment. *Oceanography* **2019**, *32*, doi:10.5670/oceanog.2019.207.

21.   Melnichenko, O.; Hacker, P.; Bingham, F.M.; Lee, T. Patterns of SSS Variability in the Eastern Tropical Pacific: Intraseasonal to Interannual Timescales from Seven Years of NASA Satellite Data. *Oceanography* **2019**, *32*, doi:10.5670/ oceanog.2019.208.

22.   Bingham, F.M.; Li, P.; Li, Z.; Vu, Q.; Chao, Y. Data management support for the SPURS Atlantic field campaign. Oceanography 2015, 28, 46–55.

23.   Bingham, F.M.; Tsontos, V.; deCharon, A.; Lauter, C.J.; Taylor, L. The SPURS-2 Eastern Tropical Pacific Field Campaign Data Collection. Oceanography 2019, 32, 142–149.

24.   Li, Z.; Bingham, F.M.; Li, P.P. Multiscale Simulation, Data Assimilation, and Forecasting in Support of the SPURS-2 Field Campaign. *Oceanography* **2019**, *32*, doi:10.5670/oceanog.2019.221.

25.   Rutledge, S.A.; Chandrasekar, V.; Fuchs, B.; George, J.; Junyent, F.; Dolan, B.; Kennedy, P.C.; Drushka, K. SEA-POL Goes to Sea. *Bulletin of the American Meteorological Society* **2019**, *100*, 2285-2301, doi:10.1175/BAMS-D-18-0233.1.

26.   Rutledge, S., A.; Chandrasekar, V.; Fuchs, B.; George, J.; Junyent, F.; Kennedy, P.; Dolan, B. Deployment of the SEA-POL C-band Polarimetric Radar to SPURS-2. *Oceanography* **2019**, *32*, doi:10.5670/oceanog.2019.212.

27. Farrar, J.T.; Rainville, L.; Plueddemann, A.J.; Kessler, W.S.; Lee, C.; Hodges, B.A.; Schmitt, R.W.; Edson, J.B.; Riser, S.C.; Eriksen, C.C., et al. Salinity and temperature balances at the SPURS central mooring during fall and winter. *Oceanography* **2015**, *28*, 56–65, doi:10.5670/oceanog.2015.06.

28. Farrar, J.T.; Plueddemann, A.J. On the Factors Driving Upper-Ocean Salinity Variability at the Western Edge of the Eastern Pacific Fresh Pool. *Oceanography* **2019**, *32*, doi:10.5670/oceanog.2019.209.

29. Yu, L. On sea surface salinity skin effect induced by evaporation and implications for remote sensing of ocean salinity. *Journal of Physical Oceanography* **2010**, *40*, 85-102.

30. Centurioni, L.R.; Hormann, V.; Chao, Y.; Reverdin, G.; Font, J.; Lee, D.K. Sea Surface Salinity Observations with Lagrangian Drifters in the Tropical North Atlantic During SPURS: Circulation, Fluxes, and Comparisons with Remotely Sensed Salinity from Aquarius. *Oceanography* **2015**, *28*, doi:10.5670/oceanog.2015.08.

31. Doney, S.C.; Glover, D.M.; McCue, S.J.; Fuentes, M. Mesoscale Variability of Sea-Viewing Wide Field-of-view Sensor (SeaWiFS) Satellite Ocean Color: Global Patterns and Spatial Scales. *Journal of Geophysical Research* **2003**, *108*, 3024, doi:10.1029/2001JC000843.

32. Clayson, C.A.; Edson, J.B.; Paget, A.; Graham, R.; Greenwood, B. Effects of Rainfall on the Atmosphere and the Ocean During SPURS-2. *Oceanography* **2019**, *32*, doi:10.5670/oceanog.2019.216.

33. Thompson, E., J.; Asher, W.E.; Jessup, A.T.; Drushka, K. High-Resolution Rain Maps from an X-band Marine Radar and Their Use in Understanding Ocean Freshening. *Oceanography* **2019**, *32*, doi:10.5670/oceanog.2019.213.

34. Rainville, L.; Centurioni, L.R.; Asher, W.E.; Clayson, C.A.; Drushka, K.; Edson, J.B.; Hodges, B.A.; Hormann, V.; Farrar, J.T.; Schanze, J.J., et al. Novel and Flexible Approach to Access the Open Ocean: Uses of Sailing Research Vessel Lady Amber During SPURS-2. *Oceanography* **2019**, *32*, doi:10.5670/oceanog.2019.219.

35. Volkov, D., L.; Dong, S.; Foltz, G.R.; Goni, G.; Lumpkin, R. Observations of Near-Surface Salinity and Temperature Structure with Dual-Sensor Lagrangian Drifters During SPURS-2. *Oceanography* **2019**, *32*, doi:10.5670/oceanog.2019.214.

36. Asher, W., E; Drushka, K.; Jessup, A.T.; Thompson, E.J.; Clark, D. Estimating Rain-Generated Turbulence at the Ocean Surface Using the Active Controlled Flux Technique. *Oceanography* **2019**, *32*, doi:10.5670/oceanog.2019.218.

37. Delcroix, T.; Chaigneau, A.; Soviadan, D.; Boutin, J.; Pegliasco, C. Eddy-Induced Salinity Changes in the Tropical Pacific. *Journal of Geophysical Research: Oceans* **2019**, *124*, 374-389, doi:10.1029/2018JC014394.

38. Jacobs, G. A.; Barron, C. N.; Rhodes, R. C., Mesoscale characteristics, J. Geophys. Res., 106(C9), 19,581–19,595, (2001), doi:10.1029/2000JC000669

39. Thyng, K. M.; Greene, C. A.; Hetland, R. D.; Zimmerle, H. M.; DiMarco, S. F. True Colors of Oceanography: Guidelines for Effective and Accurate Colormap Selection, *Oceanography* **2016**, 29(3), 9-13, doi:10.5670/oceanog.2016.66.